nature communications

Article

https://doi.org/10.1038/s41467-024-51505-4

Diurnal humidity cycle driven selective ion transport across clustered polycation membrane

Received: 14 March 2024

Accepted: 9 August 2024

Published online: 21 August 2024

Check for updates

Yuanyuan Zhao[1,2], Ju Liu[3], Gang Lu[4], Jinliang Zhang[3], Liyang Wan[5], Shan Peng[6,7], Chao Li[8] ✉, Yanlei Wang[1,3] ✉, Mingzhan Wang[9], Hongyan He[3], John H. Xin[2] ✉, Yulong Ding[10] & Shuang Zheng[6] ✉

The ability to manipulate the flux of ions across membranes is a key aspect of diverse sectors including water desalination, blood ion monitoring, purification, electrochemical energy conversion and storage. Here we illustrate the potential of using daily changes in environmental humidity as a continuous driving force for generating selective ion flux. Specifically, self-assembled membranes featuring channels composed of polycation clusters are sandwiched between two layers of ionic liquids. One ionic liquid layer is kept isolated from the ambient air, whereas the other is exposed directly to the environment. When in contact with ambient air, the device showcases its capacity to spontaneously produce ion current, with promising power density. This result stems from the moisture content difference of ionic liquid layers across the membrane caused by the ongoing process of moisture absorption/desorption, which instigates selective transmembrane ion flux. Cation flux across the polycation clusters is greatly inhibited because of intensified charge repulsion. However, anions transport across polycation clusters is amplified. Our research underscores the potential of daily cycling humidity as a reliable energy source to trigger ion current and convert it into electrical current.

Strategic utilization of environmental resources is crucial for human survival, offering a plethora of essential energy resources[1–4]. For instance, sunlight, an electromagnetic radiation, furnishes heat and, more importantly, serves as a source of solar energy[5–7]. Solar panels, laden with semiconductors like silicon, transform sunlight into electrical current, presenting a renewable, sustainable energy source for our daily consumption[5,7]. Moreover, diurnal humidity cycle, denoting the day-to-day changes in environmental moisture levels, have far-reaching effects from influencing human health and the life cycles of plants and animals to shaping broader environmental and industrial patterns[8–10]. Despite the extensive monitoring of air humidity for weather predictions, minimal efforts have been employed to harness the potential of ambient humidity cycles as a resource to benefit humanity[11–15]. Future endeavors in this direction could unlock more sustainable and eco-friendly solutions, thereby improving human life.

[1]Department of Chemistry, School of Chemistry and Life Resources, Renmin University of China, Beijing, China. [2]School of Fashion and Textiles, Hong Kong Polytechnic University, Hong Kong, China. [3]Beijing Key Laboratory of Ionic Liquids Clean Process, Institute of Process Engineering, Chinese Academy of Sciences, Beijing, China. [4]School of Energy and Environment, City University of Hong Kong, Hong Kong, China. [5]School of Computing, University of Connecticut, CT Bridgeport, USA. [6]Department of Civil Engineering, The University of Hong Kong, Hong Kong, China. [7]College of Chemistry and Materials Science, Hebei University, Baoding, China. [8]Laboratory of Bio-Inspired Smart Interfacial Science and Technology of Ministry of Education, School of Chemistry, Beihang University, Beijing, China. [9]Pritzker School of Molecular Engineering, University of Chicago, Chicago, IL, USA. [10]School of Chemical Engineering, University of Birmingham, Birmingham, UK. ✉e-mail: chaoli1994@163.com; ylwang17@ipe.ac.cn; john.xin@polyu.edu.hk; zhengshuang@iccas.ac.cn

Transmembrane ion flux, the directed movement of ions across biological membranes[1,16,17], can be precisely tailored and utilized, yielding significant benefits in diverse areas like physiological research[18,19], medical interventions, and drug discovery[9,20,21]. A prime example of this manipulation's practicality lies in osmotic energy conversion, where the migration of water from areas of low solute concentration (freshwater) towards those of higher concentration (saltwater) creates a pressure variance[22–25]. This differential pressure can be exploited to drive a turbine or generate electricity[26–29]. Therefore, the strategic control of transmembrane ion flux offers promising opportunities for human life enhancement and progressive technological evolution[29,30]. In our study, we highlight the substantial potential in using ambient humidity cycle as a spontaneous and continuous driver for selective transmembrane ion transport. We further apply this technology by integrating it into meticulously engineered microfluidic devices, which underscores the significant potential of this strategy for energy harvesting.

Results

Ambient humidity cycle-induced transmembrane ion flux

Ionic liquids (ILs), often labeled as 'non-volatile' solvents due to their resistance to evaporation, are highly valuable in various industries, including flexible electronics and energy conversion[31–33]. ILs demonstrate a spectrum of hygroscopic properties, ranging from highly hygroscopic types like imidazolium halide to less hygroscopic varieties such as imidazolium bistriflimide. For our device, we specifically chose protic ILs with chloride anions for two main reasons. Firstly, the effectiveness of our device depends on the interaction between air moisture and the IL, making the highly hygroscopic protic ILs an ideal choice. Secondly, we selected chloride as the ion to facilitate the conversion of ion current into detectable electrical output because of its effective interaction with the electrodes. The dynamics of protic ILs with moisture, involving both absorption and desorption processes, are crucially influenced by the surrounding humidity levels. During high humidity conditions, the IL tends to absorb water molecules from the air more vigorously. Conversely, in low humidity settings, the IL more readily releases water molecules back into the environment.

Our strategy is based on the daily humidity cycle, which refers to the consistent changes in humidity levels experienced over a 24-h period. This change is a continuous cycle that happens every day. When ILs are exposed to varying atmospheric humidity, they will experience a constant disequilibrium with the ambient moisture levels, indicating a perpetual shift in water content. Our device comprises a polycationic membrane sandwiched between two layers of ILs, each with a thickness of 2 mm (Fig. 1a). One of these IL layers is air-isolated (isolated layer) while the other is exposed to the atmospheric conditions (open layer). With increasing or decreasing humidity, the water content in the open layer varies, deviating from the state of the isolated layer. As the isolated layer's water content lags behind that of the open layer. This persistent discrepancy in water content across the membrane prompts ion flux, which is selectively regulated by the polycationic membrane.

In our preliminary investigations, we positioned our devices in an open-air environment while keeping them shielded from direct sunlight. We meticulously tracked and depicted the variations in humidity using data collected by hygrometer. In order to validate our hypothesis that continuous changing in humidity could consistently stimulate a transmembrane ion current, we observed the short-circuit current (I_{sc})

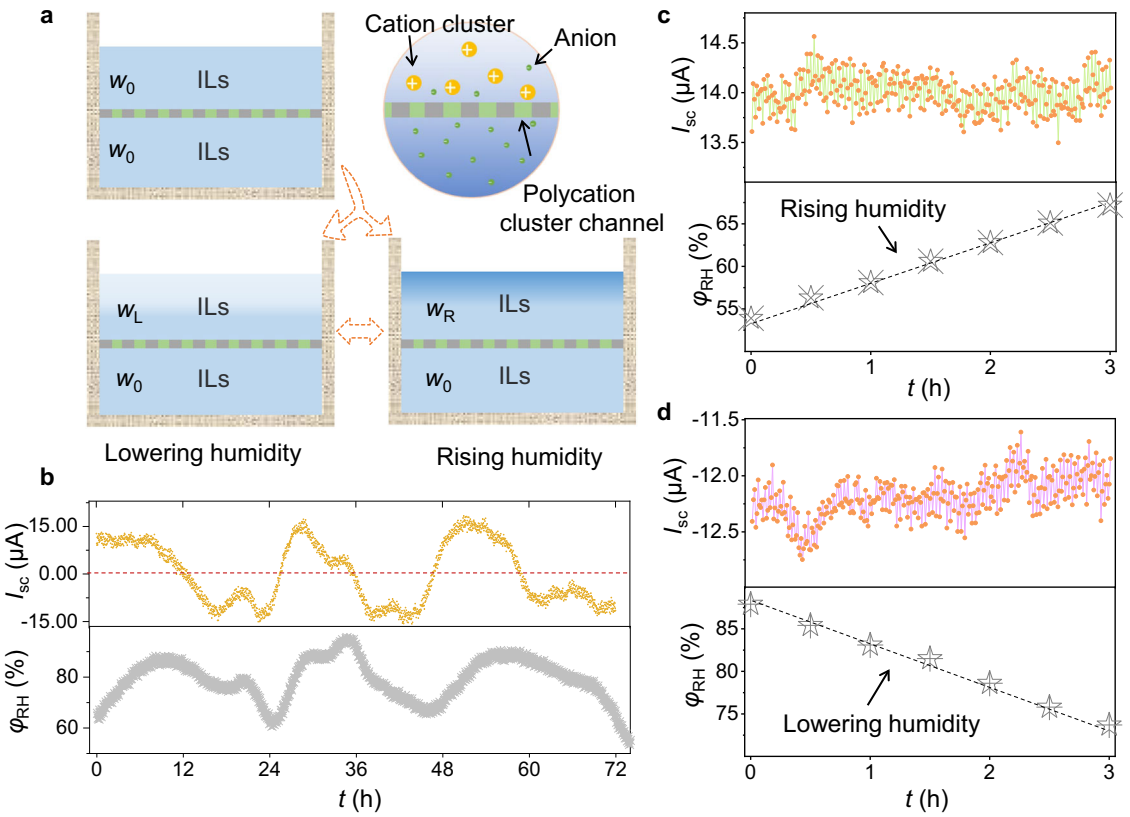

Fig. 1 | Conceptualization of transmembrane ion flux induced by humidity cycle. a Schematic representation of transmembrane concentration imbalance caused by humidity cycle triggered moisture absorption/desorption of IL. This setup comprises two IL layers enveloping a polycationic membrane, with one layer insulated from the air, while the other is left exposed for direct atmospheric interaction. As the ambient humidity is regularly fluctuating, there will be a continuous concentration imbalance. Inset represents schematic of concentration imbalance induced selective transmembrane ion flux. **b** Three-day continuous monitoring of ion current (I_{sc}) from the aforementioned system during outdoor tests, coupled with the tracking of the corresponding ambient humidity (φ_{RH}). **c**, **d** Tracking of I_{sc} during periods of increasing and decreasing ambient humidity, illustrating a strong correlation between humidity cycles and ion current.

https://doi.org/10.1038/s41467-024-51505-4

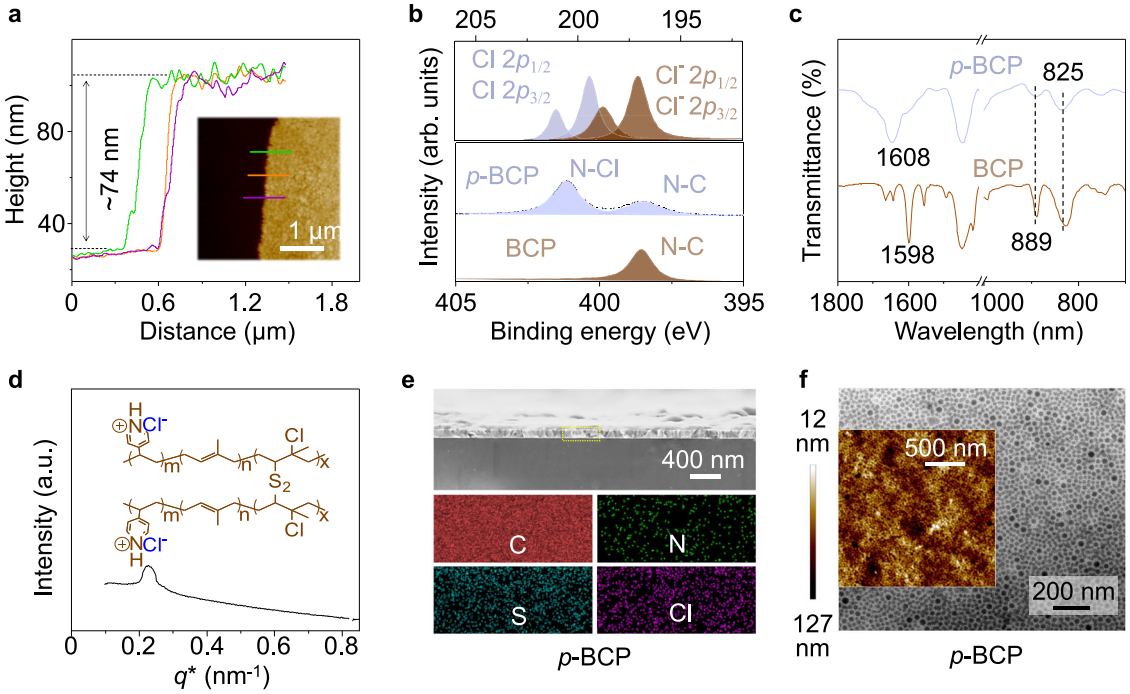

Fig. 2 | Construction of the dense polycation-cluster channels. a Height profile for the *p*-BCP membrane, showcasing an approximate thickness of 74 nm. Inset: Sectional AFM height visualization of the *p*-BCP membrane placed on a silicon wafer. **b** Detailed XPS readings for N and Cl elements in both BCP and *p*-BCP membranes. **c** FT-IR readings for both the BCP and *p*-BCP configurations. **d** 1D GI-SAXS interpretation derived from the 2D GI-SAXS layout, highlighting the periodic design. **e** SEM depiction coupled with EDS traces for the *p*-BCP membrane. **f** TEM visualization of the *p*-BCP membrane, revealing the hexagonal alignment of the polycation clusters. Inset: AFM height depiction of the *p*-BCP structure.

across our device over a period of 3 days. As presented in Fig. 1b, the setup could maintain an uninterrupted ion current with I_{sc} fluctuating from ~−14.6 to 17.9 μA. These variations corresponded to changes in relative humidity (RH) between 51.3% and 95.5%. The ongoing current output can be credited to the constant shifts in water content saturation spurred by fluctuating humidity levels, which assures that the exposed IL layer remains either unsaturated or oversaturated. We further advanced our testing by subjecting our devices to practical air conditions with either increasing or decreasing humidity levels (Fig. 1c, d). The outcomes demonstrated a reversal in ion current direction corresponding to the change in humidity trend. Above evidence collectively suggests that the ambient humidity cycle facilitates the achievement of selective transmembrane ion flux.

The diurnal humidity cycle is a universal process that occurs in the same consistent fashion throughout the world. The studies above use this daily fluctuation of environmental humidity to create a continuous and sustainable driving force for ion flux and energy conversion. While photovoltaic cells and wind turbines are limited by specific weather conditions and geography, this approach of ours does not and, therefore, can give an even flow of energy every time, independent of the day and the weather. This makes it particularly suitable for areas with consistent low-power requirements. This is well exemplified by solar panels, which perform best in high-irradiance environments and variable-free stable weather conditions (mainly constant clear weather); their output, thus, becomes quite variable. This sharply contrasts with the diurnal humidity cycle's source of energy, which is versatile, reliable, and can be applied easily to a large number of environments with utter disregard for either local weather patterns or geographic constraints.

Constructing pyridine-cluster channels

The membrane with a dense polycationic cluster configuration was developed by using a bottom-up technique, as shown in Supplementary Fig. 1. Initially, a super-thin, high-density membrane was formed through self-assembly of a block copolymer (BCP). This BCP comprised a crosslinking polyisoprene (PI) segment and an ion transport poly-4-vinylpyridine (P4VP) segment. Following that, S_2Cl_2 was used to crosslink the assembled BCP membrane, enhancing its mechanical robustness[34]. The BCP membrane, now sulfur-crosslinked (*s*-BCP), underwent an acidification process. Concurrently, chloride ions were attached to the P4VP segment due to their electrostatic attraction. This process culminated in the creation of an ultrathin, dense, and durable ion channel membrane (*p*-BCP).

The membrane thickness was measured using a cross-sectional AFM height image (Fig. 2a), revealing an average thickness of ~74 nm. Supplementary Figs. 2, 3 showed the nanostructural details of the BCP nanochannel membrane. The changes in chemical composition have been verified through XPS and FT-IR tests. Following the crosslinking with S_2Cl_2, the XPS spectra display signals for both Cl and S elements (Supplementary Figs. 4, 5). To validate the protonation of pyridine, detailed XPS spectra for N and Cl elements were taken. As depicted in Fig. 2b, N 1s peak emerges at a higher binding energy of 401.2 eV, signifying the chemical linkage between N and Cl. The detailed XPS spectra for Cl elements validate the presence of chloride post-acidification, thus confirming the creation of the Cl clusters. In the FT-IR spectra, the intensity of the double bond peak diminishes post-crosslinking, and the pyridine peak transitions from 1598 to 1608 cm^{-1} due to its protonation (Fig. 2c)[35].

The dense and regularly arranged polycation-cluster architecture is examined using GI-SAXS, SEM, AFM, and TEM methods. The 2D GI-SAXS pattern reveals a pronounced scattering void in the equatorial direction, signaling a regular vertical arrangement (Supplementary Fig. 6). Additionally, the 1D curve suggests a periodic distance of ~30.6 nm (Fig. 2d and Supplementary Fig. 7). The transmembrane ion-cluster channel structure is confirmed by the cross-sectional SEM image. The EDS patterns on the p-BCP membrane surface provide insights into its elemental makeup (Fig. 2e), aligning well with the XPS findings. The distinct transmembrane cluster arrangement is further

https://doi.org/10.1038/s41467-024-51505-4

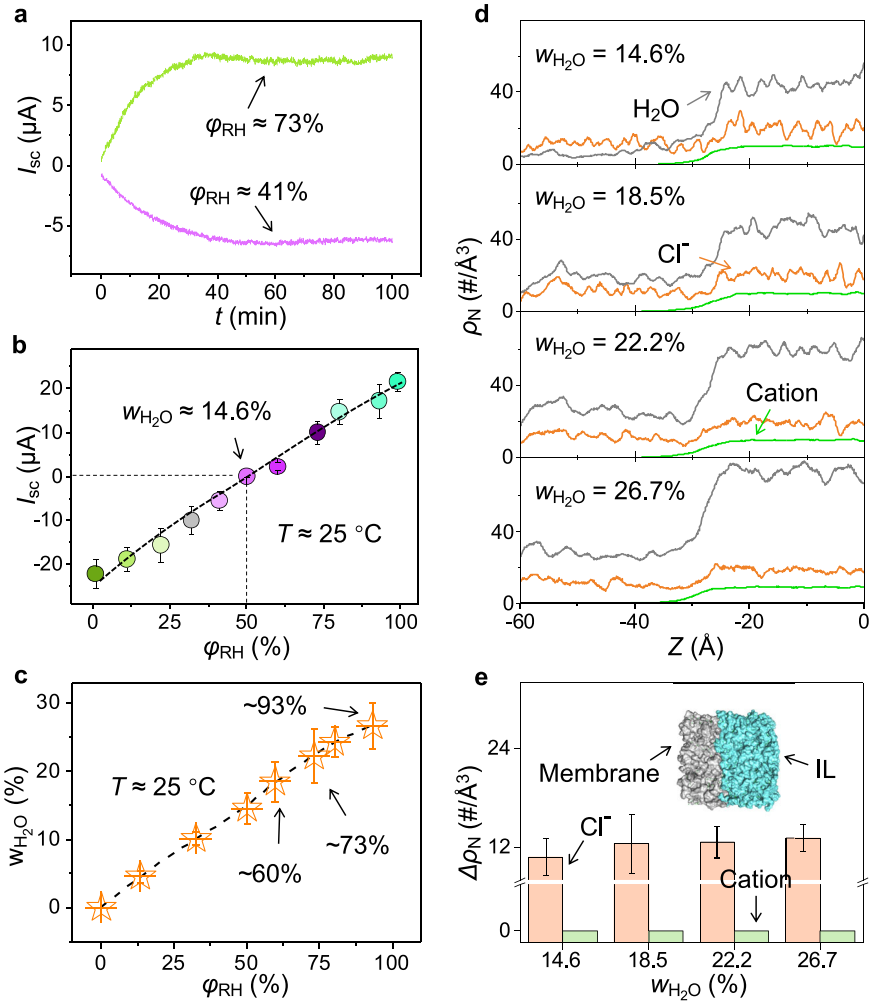

Fig. 3 | Mechanism behind the transmembrane ion flux driven by humidity variation. a The change in experimentally measured I_{sc} when subjected to surrounding RH values of ~73% and 41%. The IL layers' water content is initially balanced with an ambient RH of about 50%. **b** Measured I_{sc} mapped against the surrounding RH, ranging from as low as ~0% to as high as ~100%. **c** Equilibrium water content (w_{H_2O}) in relation to different RH values from experimental measurement. **d** Simulated distribution of cation, Cl^-, and water number density at the membrane-liquid interface, with the liquid being a mixture of ILs and water at varying concentrations. **e** Simulated comparative number density of Cl^- ion, and cation with respect to water content, with an inset of the simulation model. The error bars represent standard deviations and $n_d = 5$ for each data point.

validated by the AFM and TEM visuals (Fig. 2f). Post-acidification, the P4VP framework turns more water-attracting and swells due to electrostatic pushback (Supplementary Fig. 8). As a result, the super-thin, crosslinked membrane boasting dense pyridine clusters constructed nanochannels for selective transport of Cl^- is successfully crafted.

Humidity-driven selective anion flux across membranes with pyridine clusters

We exposed the IL layer, which had a specific water content, to various humidity levels at 25 °C and measured the ion current. This was done to uncover the mechanisms behind the humidity cycle-induced ion current (Fig. 1). In Fig. 3a, we sealed the membrane in conjunction with two IL layer, which both have a water content of about 14.6%—this is balanced with an ambient humidity of roughly 50%. When the device was subjected to RH of 73% and 41%, the equilibrium I_{sc} was found to be ~10.1 μA and −5.4 μA, respectively. This suggests that the ion flux direction can be changed by adjusting the surrounding RH.

Extending our investigation, we exposed the device to a spectrum of RH values, spanning from ~0% to ~100% (Fig. 3b). We found that increasing the difference in RH from the base 50% correspondingly increased the ion current. For instance, by raising the surrounding RH to 80%, the I_{sc} climbed to 14.8 μA. Conversely, by reducing the surrounding RH to 32%, the I_{sc} reduced to −9.9 μA. When the surrounding RH is set at 50%, the I_{sc} gravitates towards ~0 μA. These findings emphasize that the ion current has a strong association with the surrounding RH. A greater deviation from the 50% RH mark augments the difference in water content across the membrane (Fig. 3c), which in turn influences the ion current. Notably, this device works well under extreme humidity conditions, such as RH of ~0% and ~100% (Supplementary Fig. 9).

To better understand how the design of our device impacts the conversion of humidity changes into electrical current, we explored the effect of varying the thickness of the IL layer. We designed devices with the open IL layer thickness ranging from 2 to 1 mm, while maintaining the isolated layer at 2.0 mm. These devices were exposed to a relative humidity of ~73% at 25 °C to evaluate their responsiveness to humidity changes. The findings, detailed in Supplementary Fig. 10, demonstrate that a reduction in the thickness of the open layer leads to a more sensitive response, as evidenced by the output current. Specifically, when the open layer thickness is decreased from 2.0 to 1.0 mm, the time required for the current to stabilize at an equilibrium value is shortened from ~35 to ~10 min. Additionally, the equilibrium

https://doi.org/10.1038/s41467-024-51505-4

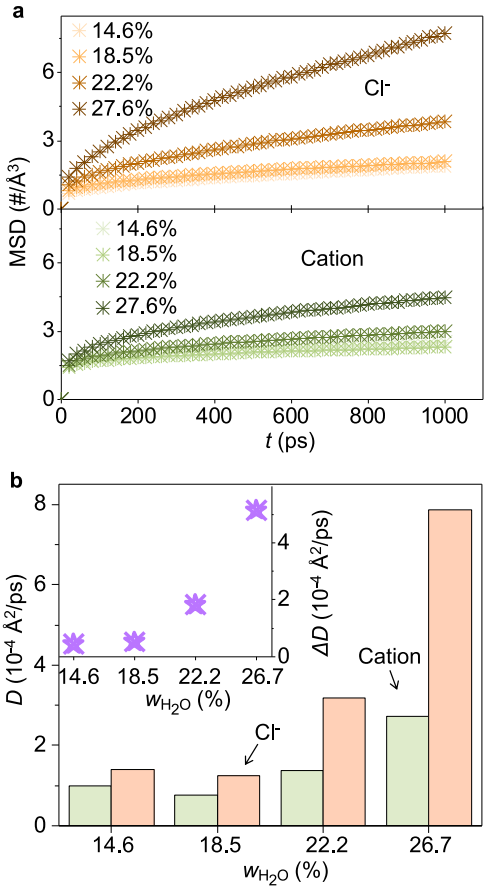

Fig. 4 | Simulated ion diffusion characteristics at the membrane interface. **a** Analysis of the mean square displacement (MSD) for Cl^- and cations in systems with varying water content. **b** Evaluation of the self-diffusion coefficients for chloride ions and cations relative to water content. The inset shows the variance in self-diffusion coefficients between the two types of ions.

current increases from 10.1 to 12.9 μA. This improvement is attributed to the decreased diffusion distance and enhanced rate of moisture absorption. A thinner IL layer means water molecules have a shorter path to travel from the air to the membrane interface, speeding up permeation and thereby boosting water absorption. Furthermore, this reduction in thickness increases the surface area-to-volume ratio at the interface where the air contacts the IL, allowing a greater portion of the IL to interact directly with ambient air, which accelerates moisture exchange.

To elucidate the origin of ion current, we examined the distribution of IL species at the liquid-membrane interface on a molecular scale, using full-atomistic molecular dynamics simulations. These simulations revealed that chloride ions Cl^- readily penetrate the membrane's inner regions, while cations predominantly remain in the liquid phase (as illustrated in Fig. 3d). Additionally, we explored the impact of water content on ion distribution, observing in Fig. 3e that the average number density of Cl^- and cations varies with water content. Notably, the number density of Cl^- increases with rising water content and significantly exceeds that of the cations. We also investigated the diffusive behavior and properties of ILs through mean square displacement (MSD) analysis (Fig. 4a, b). As water content increases, the self-diffusion coefficient (SDC) of Cl^- rises more rapidly than that of the cations, indicating that Cl^- diffuses faster than cations. The aggregation and rapid diffusion of Cl^- within the membrane support our theory that Cl^- plays a dominant role in the entire ion current generation process.

Hydrophobic interactions enhanced selective flux across pyridine clusters

Beyond our investigation of the membrane, we have also explored how the IL layers affect ion flux and ion current generation. The particular IL under scrutiny possesses a hydrophobic chain that is terminated by ammonium at both ends. These hydrophobic chains can cluster together to reduce exposure to polar or charged entities. Such a gathering of ions in the IL, termed ion clustering, results in them grouping together rather than distributing uniformly. This creates regions within the IL where ions are more densely concentrated.

To elucidate the impact of hydrophobic chain length on transmembrane ion movement, we synthesized three polyether amine fatty acid ILs: $[PEA_{230}]Cl_2$, $[PEA_{400}]Cl_2$, and $[PEA_{2000}]Cl_2$. Protic ILs have good ionic conductivity due to mobile ions[36], making them ideal for electrochemical devices like batteries and supercapacitors. So we use PEA ILs to reduce internal electrical resistance of the IL layers. In addition, PEA ILs is highly hygroscopic, absorbing moisture from the environment[37], which is crucial for our device that generates ion flux through humidity cycles. Their polyether backbone also provides flexibility for varying ion transport, ensuring high ion selectivity. Additionally, they offer good thermal stability[38,39]. In contrast, common cations in aprotic ILs, such as imidazolium and pyridinium, cannot dissociate protons and lack these advantages.

The structures of these ILs were confirmed using ^{1}H NMR and FTIR spectroscopy, as illustrated in Fig. 5a, b, and Supplementary Fig. 11. The ^{1}H NMR spectra revealed the disappearance of the $-NH_2$ peak at 1.48 ppm in PEA, replaced by a new NH_3^+ peak at 8.13 ppm. Similarly, the FTIR spectra showed the characteristic $-CH_2$ and $-CH_3$ stretching vibration peaks at 2900 cm^{-1}, along with new peaks at 1460 and 1380 cm^{-1} corresponding to $-CH_2$ and $-CH_3$ groups. The peak at 1115 cm^{-1} was identified as the stretching vibration of the C–O–C bond. These findings collectively confirm the successful synthesis of the three PEA ILs.

Power density (P_d) is widely recognized as the criterion for assessing energy harvesting potential. We integrated the aforementioned ILs into our apparatus and determined the output power density when subject to a constant ambient RH of ~73%. Initially, the water content in the isolated and open IL layers were both balanced with an air humidity of about 50%. We used the generator (with an effective area, A) to power external resistive loads (R_e) and recorded the resultant current (I_e). As depicted in Fig. 5c, the power density, defined as $P_d = I_e^2 R_e/A$, peaks with an R_e of about 10 kΩ for IL with n value of 5. We would like to highlight that our device demonstrates a significant advancement in both power density and current density compared to other devices that generate electricity triggered by air moisture (Supplementary Fig. 12). Stability is another crucial factor affecting the practical application of our device. To evaluate its stability, we continuously monitored the I_{sc} over a period of ~4 weeks (under the same condition with Fig. 3a, RH of ~73%). The results, presented in Supplementary Fig. 13, demonstrate that our device can operate continuously for 4 weeks without obvious degradation in performance.

Additionally, we analyzed the variation in power density with respect to n, as illustrated in Fig. 5c–e demonstrating an optimal n value. The length of the side chains significantly impacts power generation: increasing n to 32 or reducing it to two both result in a simultaneous decrease in power density and I_{sc}. Based on Fig. 5f, altering the length of the side chain, either by increasing or decreasing, leads to a reduction in the equilibrium water molar ratio. For $n = 5$, the water-to-IL ratio stands at around 6:1. This is more than the ratios for $n = 2$ (5:1) and $n = 32$ (3:1). The capability to take in more water molecules contributes to a pronounced difference in water content across the membrane, bolstering selective ion flux and subsequently, a greater power output. In addition, as the IL absorbs more water, it

https://doi.org/10.1038/s41467-024-51505-4

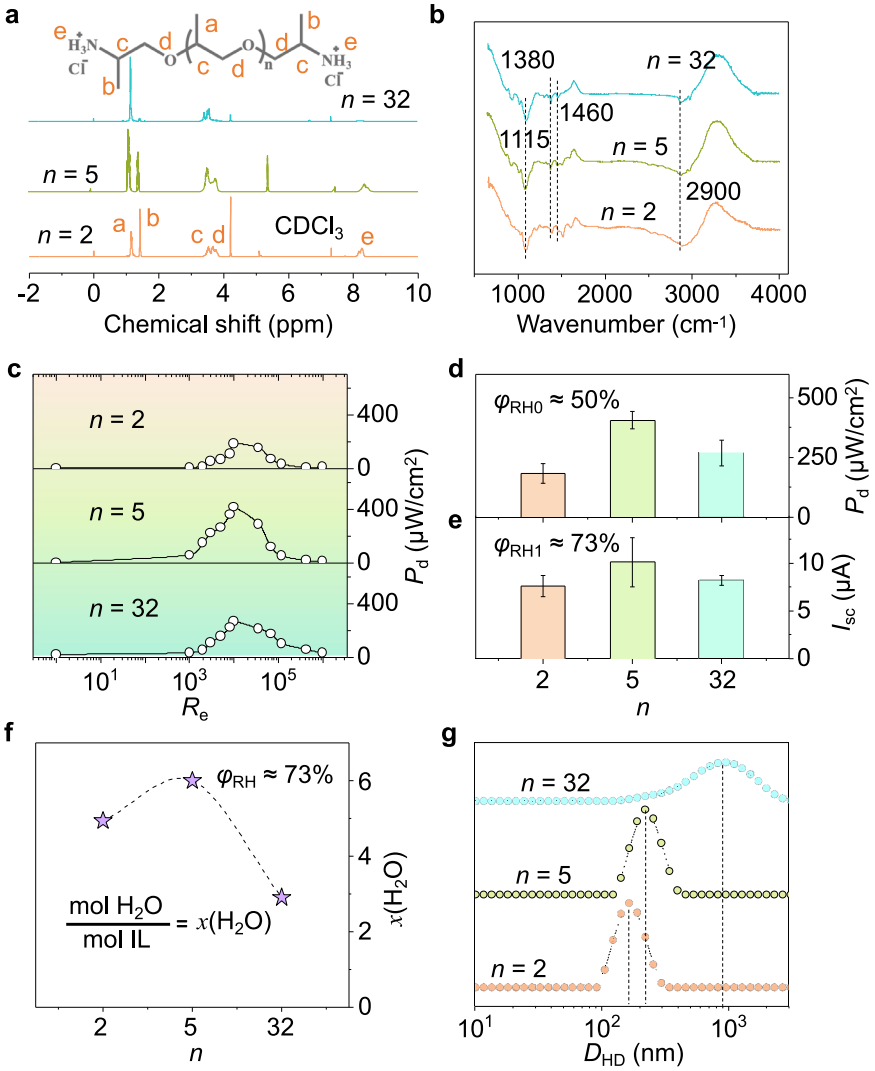

Fig. 5 | IL clustering enhanced selective ion flux. a, **b** ^{1}H NMR and FTIR spectra of the ILs with $n = 2$, 5, and 32. **c** Power density chart for ILs with n values of 2, 5, and 32, plotted against external resistances spanning from 1 to 10^6 Ω. **d**, **e** Overview of the peak power density and the associated I_{sc}. **f** Equilibrium water molar ratio at an ambient humidity of ~73% at 25 °C. **g** The size distribution of cluster in ILs-water mixture system for $n = 2$, 5, and 32. The error bars represent standard deviations and $n_d = 5$ for each data point.

enhances ion dissociation, thus increasing the number of free ions within the system. These liberated ions can move more freely throughout the IL and play a crucial role in increasing current generation, as a greater number of ions are available to engage in the transmembrane ion flux. This aligns with the operational mechanism depicted in Fig. 3b. Nonetheless, it's worth pointing out that even though IL with $n = 2$ exhibits a substantially higher water molar ratio than IL with $n = 32$, their power densities and corresponding I_{sc} values are contrary (Fig. 5d, e).

We attribute the observed discrepancy to ion clustering, as depicted in Fig. 5g. Ion clustering is the phenomenon where ions in a solution come together to create bigger entities known as clusters. In our study, these clusters of cations arise due to the hydrophobic interactions linked to the length of the side chains. Specifically, $[PEA_{2000}]^{2+}$ shows a more pronounced propensity to aggregate compared to $[PEA_{230}]^{2+}$, leading to the formation of larger cation clusters. The larger clusters with stronger charges experience significant electrostatic repulsion from the similarly charged polycationic membrane. This repulsion prevents the clusters from easily penetrating the membrane, thereby enhancing the overall current generation in the device.

Scalability of the polycation membrane for energy conversion and storage

Finally, we demonstrate the practicality and scalability of using humidity cycle-driven selective ion flux as a renewable energy source, by connecting this device in series or parallel. Initially, we constructed this device on microfluidic platforms (Supplementary Fig. 14a). The design of this microfluidic chip includes two arrays of pores, separated by a central membrane. IL ($n = 5$) was infused into these pores, and a sealing membrane was used to isolate one side from the air, leaving the opposite side exposed. We introduced Ag/AgCl to measure the ion current. As shown in Supplementary Fig. 14b, we observed that when the pores (each 300 μm in diameter) are connected in parallel, they produce a short-circuit current of ~2700 μA. This result indicates that our device can be effectively scaled in a parallel arrangement. Additionally, we evidence that a single unit can efficiently charge capacitors ranging from 1 to 1000 μF in a brief period (around 2 min), as depicted in Supplementary Fig. 14c. Then, we engineered a circuit, shown in Supplementary Fig. 15, which consists of 16 capacitors connected in series, designed for energy storage. This setup successfully generated a voltage up to ~2.21 V (Supplementary Fig. 14d), sufficient to power a green LED requiring about 1.8 V. Collectively, these findings establish

the potential of humidity cycles as a viable and eco-friendly energy resource, which is not heavily dependent on specific geographic or climatic conditions.

Discussion

In conclusion, we have strategically utilized the daily variations in atmospheric humidity to stimulate a persistent ion current. We believe that this selective ion transport is facilitated by the polycationic membrane's ability to effectively repel cationic clusters formed due to the hydrophobic interactions of alkyl chains, while concurrently permitting anion transportation. A singular device was able to achieve a substantial power density of ~405.9 μW/cm^2. To demonstrate the practical application of this design, we integrated this device onto fluidic chips, which were then able to generate a voltage of ~2.21 V.

Looking forward, the capability to scale up these devices and integrate them onto fluidic chips opens the door to miniaturization and mass production. This holds promising implications for a myriad of applications, from powering remote environmental sensors to fueling wearable health devices[40–45]. The technology presents a virtually uninterrupted power source, a feature particularly beneficial for wearables that demand round-the-clock operation. Furthermore, this technology's influence extends beyond just power generation. The humidity cycles' ability to facilitate selective ion transport could provide valuable insights into nanotechnology, notably in specialized fields such as drug delivery systems and biosensing[30,46–48].

Methods

Materials

Poly(1,4-isoprene)-b-poly(4-vinylpyridine) ($PI_{30,000}$-*b*-$P4VP_{11,700}$, Polymer Source, PDI = 1.06), polystyrene sulfonic acid sodium (PSS, Alfa, Mw = 70,000), sulfur monochloride (S_2Cl_2), carbon disulfide (CS_2), acetone, and toluene (all from Beijing Chemical Reagents Co.) were utilized as received. PEAX (Poly(propylene glycol) bis(2−aminopropyl ether) with molecular weights of ~230, 400, and 2000 g/mol, is sourced from Aladdin. Additionally, hydrochloric acid with a concentration of 36.0% to 38.0% was acquired from Kunshan Jincheng Chemical Reagent Co., Ltd. All experiments were conducted using deionized water.

Preparation of the pronated block copolymer (BCP) membrane

The fabrication of the protonated BCP membrane began with the ultrasonic cleaning of a silicon wafer using acetone. Subsequently, a 4 wt% PSS solution was spin-coated onto the wafer at 3000 rpm for 1 min. The coated membrane was then dried under a nitrogen atmosphere for 30 min. Following this, a 2 wt% BCP solution in toluene was spin-coated onto the PSS layer to create the nanochannel membrane. Once fully dried, the membrane underwent crosslinking with S_2Cl_2 vapor inside a sealed container. Excess S_2Cl_2 and sulfur were removed using CS_2. The membrane was then immersed in water to eliminate the PSS sacrificial layer. The final step involved protonating the crosslinked membrane in a 1.0 M hydrochloric acid (HCl) solution to enhance the charge density of the P4VP nanochannels, resulting in a self-standing ion-cluster channel membrane.

X-ray photoelectron spectroscopy (XPS)

Surface chemical analysis was conducted using a Thermo Scientific K-Alpha at a pressure of 5E-7 mbar, using a monochromatic Al Kα X-ray source ($h\nu$ = 1486.6 eV). XPS readings were taken at normal emission at ambient conditions.

Grazing-incidence small-angle X-ray scattering (GI-SAXS)

The alignment of nanochannels and the periodicity of various membranes were verified using GI-SAXS. These measurements were performed using a Xeuss 3.0 system from Xenocs SA, France. The system utilized Cu Kα X-ray radiation with a wavelength of 1.5418 Å. Detection of the scattering signals was achieved with a Pilatus 300 K CCD detector by DECTRIS, Swiss, which has a 487 × 619 pixel resolution and a pixel size of 172 × 172 μm^2. The detector was placed at a distance of 1800 mm from the samples and the grazing incidence angle was maintained between 0.2° and 0.3°.

Transmission electron microscopy (TEM)

The nanostructure of various membranes was examined using TEM techniques. Images were captured on a JEM-2100 TEM at an accelerating voltage of 200 kV. For sample preparation, a 0.5 wt% solution of BCP in toluene was deposited onto a copper grid. This membrane was then dried in a nitrogen atmosphere for 30 min. Post-drying, the polyimide phase of the *s*-BCP membrane was specifically stained using osmium tetroxide (OsO4) for 5 min to enhance visibility. Similarly, the P4VP phase of the *p*-BCP membrane underwent selective staining with iodine vapor for 20 min, which served to increase the contrast in the TEM images.

Scanning electron microscopy (SEM)

The structure of the nanochannels traversing the membrane was verified using a ZEISS Gemini 300 scanning electron microscope, equipped with a Schottky field emission electron source, operating at an acceleration voltage of 5 kV. The nanochannel membrane, after protonation, was placed on a silicon substrate. To reveal its cross-sectional structure, the sample was fractured in liquid nitrogen. The distribution of elements within the membranes was analyzed using SEM-based elemental mapping (Smartedx).

Fourier-transform infrared spectroscopy (FT-IR)

The cross-linking and protonation states of the membrane were validated through FT-IR analysis. These FT-IR tests were carried out using a Bruker Vertex70 instrument, which scanned in a range from 400 to 4000 cm^{-1}.

Contact angle

The surface wettability of prepared membrane surfaces was measured by the optical contact angle meter system (OCA40Micro, Dataphysics Instruments GmbH, Germany). At room temperature, 2 μL of ionized water was dropped onto the membrane surfaces. The contact angles were calculated by the tangent method.

Atomic force microscopy (AFM) detections

The surface textures and thickness of the membrane in air conditions were characterized using AFM. This was performed with a Bruker Dimension Icon AFM device utilizing ScanAsyst mode in air, with a scanning frequency of 0.977 Hz.

Preparation of the ILs

ILs PEA-Cl, specifically $[PEA_{230}]Cl_2$, $[PEA_{400}]Cl_2$, and $[PEA_{2000}]Cl_2$, were synthesized using the acid-base neutralization method[49]. The process began by adding PEAX and hydrochloric acid into a round-bottom flask in a 1:2 molar ratio. This mixture was then stirred continuously at 30 °C for 24 h. After this period, the resultant PEA-Cl ILs were subjected to a drying process under vacuum conditions for 48 h at 50 °C, to effectively remove any trace amounts of water.

Characterization of ILs

The ^{1}H NMR spectra for the ILs were obtained using a Bruker AVANCE III HD 600 NMR spectrometer. The FTIR spectra of the ILs were recorded with a Thermo Scientific Nicolet iS50 spectrometer. For dynamic light scattering (DLS) analysis, a Malvern Nano ZS-90 particle size analyzer was employed, equipped with a 4.0 mW solid-state He-Ne laser, operating at a wavelength of 633 nm. Prior to analysis, all IL samples were filtered through a 0.45 μm hydrophilic polyvinylidene fluoride (PVDF) membrane filter to eliminate dust particles.

Molecular dynamics simulations

All the simulations employed Amber18 to explore the molecular mechanisms of humidity cycles driving ion flux across membranes[50]. The initial setup was created with the PACKMOL package, including 195 membrane molecules and 523 molecules of IL, specifically D400 polyether amine chloride[51]. Water content in the IL phase was varied to achieve concentrations of 14.6%, 18.5%, 22.2%, and 26.7% by adding different amounts of water molecules. The simulation box measured around 98 × 88 × 200 Å[52]. For water molecules, the TIP3P model was used, while the General Amber Force Field 2 described other species[46,52]. Simulations were conducted in the NVT ensemble at 298 K. Each simulation lasted 100 ns with a 2 fs time step. Analysis was focused on the final 20 ns of each run, where parameters such as density distribution and MSD were calculated.

Data availability

The data supporting the findings of this study are available within the paper and its Supplementary Information. Other relevant data are available from the corresponding author on request.

Code availability

The calculations for selective transmembrane ion flux, as described in the Methods, have been processed and analyzed by the in-house software "ionic liquid database and analysis software" developed by the authors[47,48], which are available from the corresponding author on request.

References

1. Siria, A. et al. Giant osmotic energy conversion measured in a single transmembrane boron nitride nanotube. *Nature* **494**, 455–458 (2013).
2. Yang, C., Huang, Y., Cheng, H., Jiang, L. & Qu, L. Rollable, stretchable, and reconfigurable graphene hydroelectric generators. *Adv. Mater.* **31**, e1805705 (2019).
3. Li, S. Y. et al. Manipulating the triboelectric surface charge density of polymers by low-energy helium ion irradiation/implantation. *Energy Environ. Sci.* **13**, 896–907 (2020).
4. Wei, D., Yang, F. Y., Jiang, Z. H. & Wang, Z. L. Flexible iontronics based on 2D nanofluidic material. *Nat. Commun.* **13**, 4965 (2022).
5. Yoo, J. J. et al. Efficient perovskite solar cells via improved carrier management. *Nature* **590**, 587–593 (2021).
6. Service, R. F. Solar energy gets flexible. *Science* **378**, 588–591 (2022).
7. You, S. et al. Bifunctional hole-shuttle molecule for improved interfacial energy level alignment and defect passivation in perovskite solar cells. *Nat. Energy* **8**, 515–525 (2023).
8. Arazoe, H. et al. An autonomous actuator driven by fluctuations in ambient humidity. *Nat. Mater.* **15**, 1084–1089 (2016).
9. Peng, S. et al. Low-grade wind-driven directional flow in anchored droplets. *Proc. Natl. Acad. Sci. USA* **120**, e2303466120 (2023).
10. Yang, C. et al. Transfer learning enhanced water-enabled electricity generation in highly oriented graphene oxide nanochannels. *Nat. Commun.* **13**, 6819 (2022).
11. Wang, H. et al. Bilayer of polyelectrolyte films for spontaneous power generation in air up to an integrated 1000 V output. *Nat. Nanotechnol.* **16**, 811–819 (2021).
12. Liu, X. et al. Power generation from ambient humidity using protein nanowires. *Nature* **578**, 550–554 (2020).
13. Huang, Y. et al. Interface-mediated hydroelectric generator with an output voltage approaching 1.5 volts. *Nat. Commun.* **9**, 4166 (2018).
14. Cheng, H. et al. Spontaneous power source in ambient air of a well-directionally reduced graphene oxide bulk. *Energy Environ. Sci.* **11**, 2839–2845 (2018).
15. Wang, P. F., Xu, J. X., Wang, R. Z. & Li, T. X. Pathways for continuous electricity generation from ambient moisture. *Matter* **6**, 19–22 (2023).
16. Esfandiar, A. et al. Size effect in ion transport through angstrom-scale slits. *Science* **358**, 511–513 (2017).
17. Feng, J. D. et al. Single-layer MoS2 nanopores as nanopower generators. *Nature* **536**, 197–200 (2016).
18. Kefauver, J. M., Ward, A. B. & Patapoutian, A. Discoveries in structure and physiology of mechanically activated ion channels. *Nature* **587**, 567–576 (2020).
19. Chen, W. et al. Cascade-heterogated biphasic gel iontronics for electronic-to-multi-ionic signal transmission. *Science* **382**, 559–565 (2023).
20. Zhang, H. C., Li, X. Y., Hou, J., Jiang, L. & Wang, H. T. Angstrom-scale ion channels towards single-ion selectivity. *Chem. Soc. Rev.* **51**, 2224–2254 (2022).
21. Itoh, Y. et al. Ultrafast water permeation through nanochannels with a densely fluorous interior surface. *Science* **376**, 738–743 (2022).
22. Laucirica, G., Toimil-Molares, M. E., Trautmann, C., Marmisolle, W. & Azzaroni, O. Nanofluidic osmotic power generators - advanced nanoporous membranes and nanochannels for blue energy harvesting. *Chem. Sci.* **12**, 12874–12910 (2021).
23. Wang, L. D. et al. Fundamental transport mechanisms, fabrication, and potential applications of nanoporous atomically thin membranes. *Nat. Nanotechnol.* **12**, 509–522 (2017).
24. Wang, C. et al. Ultrathin self-standing covalent organic frameworks toward highly-efficient nanofluidic osmotic energy generator. *Adv. Funct. Mater.* **32**, 2204068 (2022).
25. Wu, C. R. et al. Biomimetic temperature-gated 2D cationic nanochannels for controllable osmotic power harvesting. *Nano Energy* **76**, 105113 (2020).
26. Zhao, Y. Y. et al. Robust sulfonated poly (ether ether ketone) nanochannels for high-performance osmotic energy conversion. *Natl Sci. Rev.* **7**, 1349–1359 (2020).
27. Li, C. et al. Large-scale, robust mushroom-shaped nanochannel array membrane for ultrahigh osmotic energy conversion. *Sci. Adv.* **7**, eabg2183 (2021).
28. Zhang, Z., Wen, L. P. & Jiang, L. Nanofluidics for osmotic energy conversion. *Nat. Rev. Mater.* **6**, 622–639 (2021).
29. Chen, C. et al. Bio-inspired nanocomposite membranes for osmotic energy harvesting. *Joule* **4**, 247–261 (2020).
30. Acar, E. T., Buchsbaum, S. F., Combs, C., Fornasiero, F. & Siwy, Z. S. Biomimetic potassium-selective nanopores. *Sci. Adv.* **5**, eaav2568 (2019).
31. Gao, N. W. et al. Crystal-confined freestanding ionic liquids for reconfigurable and repairable electronics. *Nat. Commun.* **10**, 547 (2019).
32. Cao, Z. Q., Liu, H. L. & Jiang, L. Transparent, mechanically robust, and ultrastable ionogels enabled by hydrogen bonding between elastomers and ionic liquids. *Mater. Horiz.* **7**, 912–918 (2020).
33. Ankit et al. High-k, ultrastretchable self-enclosed ionic liquid-elastomer composites for soft robotics and flexible electronics. *ACS Appl. Mater. Interfaces* **12**, 37561–37570 (2020).
34. Liu, G. J., Yan, X. H. & Duncan, S. Polystyrene-block-polyisoprene nanofiber fractions. 1. preparation and static light-scattering study. *Macromolecules* **35**, 9788–9793 (2002).
35. Vidinha, P. et al. Enhanced biocatalytic activity of ORMOSIL-encapsulated cutinase: the matrix structural perspective. *J. Phys. Chem. C* **112**, 2008–2015 (2008).
36. Greaves, T. et al. Protic ionic liquids: evolving structure-property relationships and expanding applications. *Chem. Rev.* **115**, 11379–11448 (2015).
37. Yuan, X. et al. Ionic liquids enable highly efficient Knoevenagel reaction by dual-responsive emulsion microreactor. *Chem. Eng. J.* **451**, 138941 (2023).
38. Liu, X. et al. Efficient and sustainable separation of oil from oily wastes using acid-base switchable ionic liquid system. *Chem. Eng. Res. Des.* **202**, 347–354 (2024).

39. Zaitsau, D. H. et al. Structure–property relationships in ionic liquids: Influence of branched and cyclic groups on vaporization enthalpies of imidazolium-based Ils. *J. Chem. Thermodyn.* **93**, 151–156 (2016).
40. Miao, W. et al. Micro-/nano-voids guided two-stage film cracking on bioinspired assemblies for high-performance electronics. *Nat. Commun.* **10**, 3862 (2019).
41. Jayathilaka, W. A. D. M. et al. Significance of nanomaterials in wearables: a review on wearable actuators and sensors. *Adv. Mater.* **31**, 1805921 (2019).
42. Aaryashree et al. Recent developments in self-powered smart chemical sensors for wearable electronics. *Nano Res.* **14**, 3669–3689 (2021).
43. Sabbagh, B., Park, S. & Yossifon, G. Microvalve-based tunability of electrically driven ion transport through a microfluidic system with an ion-exchange membrane. *Anal. Chem.* **95**, 6514–6522 (2023).
44. Lu, G. et al. Nano-confined supramolecular assembly of ultrathin crystalline polymer membranes for high-performance nanofiltration. *Adv. Funct. Mater.* **34**, 2309913 (2023).
45. Zhao, Y. et al. Capillary condensation mediated fluidic straining for enhanced bacterial inactivation. *Adv. Funct. Mater.* **34**, 2314581 (2024).
46. Wang, J. M., Wolf, R. M., Caldwell, J. W., Kollman, P. A. & Case, D. A. Development and testing of a general amber force field. *J. Comput. Chem.* **25**, 1157–1174 (2004).
47. Zhang S. J., Zhou Q., Lu X. M., Wang X. X., Lu C. H. "IPE Ionic Liquid Database", Institute of Process Engineering, Chinese Academy Sciences, Beijing, 100190. http://ildate.ilct.com.cn/.
48. Zhang S. J., Zhou Q., Lu X. M., Song Y. T., Wang X. X. *Physicochemical Properties of Ionic Liquid Mixtures* (Springer, 2017).
49. Yuan, X. Q. et al. Smart ionic liquid/water mixture system with dual stimuli-response to temperature and CO. *Nano Res.* **16**, 4152–4159 (2023).
50. Case, D.A.B.-S., I. Y. et al. University of California, San Francisco: San Francisco, CA. *AMBER 2018*.
51. Martínez, L., Andrade, R., Birgin, E. G. & Martínez, J. M. PACKMOL: a package for building initial configurations for molecular dynamics simulations. *J. Comput. Chem.* **30**, 2157–2164 (2009).
52. Jorgensen, W. L., Chandrasekhar, J., Madura, J. D., Impey, R. W. & Klein, M. L. Comparison of simple potential functions for simulating liquid water. *J. Chem. Phys.* **79**, 926–935 (1983).

Acknowledgements

S.Z. acknowledges financial support from the University of Hong Kong (2201100473). H.H. and Y.W. thank the funding from National Natural Science Foundation of China (22278401 and 22178344), and the independent research project of Zhengzhou Institute of Emerging Industrial Technology (ZZLX2022002). C.L. acknowledges funding from the Postdoctoral Fellowship Program of CPSF (GZB20230923), the China Postdoctoral Science Foundation (2024M754049).

Author contributions

S.Z. conceived and led the project. Y.Z. designed the experiments and drafted the manuscript. Y.Z. and G.L. conducted the research. C.L. designed the membrane, Y.W., J.L., H.H., and J.Z. synthesized the ILs, conducted and drafted the simulations. Y.D., L.W., S.P., H.H., and M.W. contributed to this work by analyzing the data and revising the manuscript. Y.Z., J.L., and G.L. contributed equally. C.L., Y.W., J.X., and S.Z. supervised the project. All authors discussed the results and commented on the manuscript.

Competing interests

The authors declare no competing interests.

Additional information

Supplementary information The online version contains supplementary material available at https://doi.org/10.1038/s41467-024-51505-4.

Correspondence and requests for materials should be addressed to Chao Li, Yanlei Wang, John H. Xin or Shuang Zheng.

Peer review information *Nature Communications* thanks the anonymous reviewers for their contribution to the peer review of this work. A peer review file is available.